

Interplay of inertia and deformability on rheological properties of a suspension of capsules

Timm Krueger^{1,2†}, Badr Kaoui^{3,4}
and Jens Harting^{4,5}

¹School of Engineering, University of Edinburgh, The King's Buildings, Mayfield Road, EH9 3JL Edinburgh, United Kingdom

²Centre for Computational Science, University College London, 20 Gordon Street, WC1H 0AJ London, United Kingdom

³Physikalisches Institut, Universität Bayreuth, Theoretische Physik I, 95440 Bayreuth, Germany

⁴Department of Applied Physics, Eindhoven University of Technology, P. O. Box 513, 5600 MB Eindhoven, The Netherlands

⁵Faculty of Science and Technology, Mesa+ Institute, University of Twente, 7500 AE Enschede, The Netherlands

(Received ?; revised ?; accepted ?. - To be entered by editorial office)

The interplay of inertia and deformability has a substantial impact on the transport of soft particles suspended in a fluid. However, to date a thorough understanding of these systems is still missing and only a limited number of experimental and theoretical studies is available. We combine the finite-element, immersed-boundary and lattice-Boltzmann methods to simulate three-dimensional suspensions of soft particles subjected to planar Poiseuille flow at finite Reynolds numbers. Our findings confirm that the particle deformation and inclination increase when inertia is present. We observe that the Segré-Silberberg effect is suppressed with respect to the particle deformability. Depending on the deformability and strength of inertial effects, inward or outward lateral migration of the particles takes place. In particular, for increasing Reynolds numbers and strongly deformable particles, a hitherto unreported distinct flow focusing effect emerges which is accompanied by a non-monotonic behaviour of the apparent suspension viscosity and thickness of the particle-free layer close to the channel walls. This effect can be explained by the behaviour of a single particle and the change of the particle collision mechanism when both deformability and inertia effects are relevant.

1. Introduction

Fluid inertia and particle deformability — quantified by the Reynolds (Re) and capillary (Ca) numbers, respectively — have significant impact on the individual and collective motion of particles in suspension. For example, most deformable particles in a viscous flow tend to migrate laterally *towards* the centreline of a Poiseuille flow, creating a depletion layer near the confining walls. However, it is also known that deformable droplets (Leal 1980) and vesicles (Farutin & Misbah 2013) can migrate *away* from the centreline under certain conditions. Rigid particles at intermediate Reynolds numbers which are originally located near the centreline migrate towards the walls until the inertial lift is balanced by the wall repulsion. While most studies in the literature focus on

† Email address for correspondence: timm.krueger@ed.ac.uk

the effect of either inertia or deformability separately, we address their combination and as such aim at answering the following question: *what is the interplay between inertia and deformability in a flowing suspension?*

A deep understanding of the flow of suspensions and their components is of fundamental practical importance. For example, lateral migration of particles is exploited for separating and sorting out cancer cells from healthy blood cells in lab-on-chip devices (Hur *et al.* 2011; Tanaka *et al.* 2012; Geislinger *et al.* 2012; Krüger *et al.* 2013). The macroscopic viscosity of a suspension, which is of relevance for systems like waste water sewage and industrial production lines, depends on its microscopic composition and particle distribution. The ultimate goal is to predict the rheology of a suspension based on its microscopic properties, such as local particle concentration and particle deformation.

About 50 years ago, Segré & Silberberg (1962*a,b*) discovered that rigid particles in inertial tube flow (with tube radius r) have equilibrium positions at a radial distance of about $0.6r$. This equilibrium lateral position results from balancing the confinement induced repulsive wall force and shear rate gradients. Matas *et al.* (2004) later extended the experiments to larger Reynolds numbers and observed the formation of an additional inner annulus. Particles initially located in off-equilibrium positions tend to show cross-streamline migration until they reach an equilibrium position (Humphry *et al.* 2010). Understanding the lateral migration of rigid particles in the presence of inertia is a difficult problem. The existing asymptotic theory (Schonberg & Hinch 1989; Asmolov 1999) explaining this behaviour is only valid for weak confinement and small particle Reynolds numbers, although the channel Reynolds number can be large.

Numerical lattice-Boltzmann simulations of a single particle and dilute suspensions in the regime $100 \leq Re \leq 1000$ showed that multi-body interactions play a crucial role in the formation of inner equilibrium positions (Chun & Ladd 2006). In strongly confined rectangular flows, rigid particles experience inertial focusing and are aligned in one or multiple lines, depending on the particle volume fraction and the channel aspect ratio (Humphry *et al.* 2010). These findings demonstrate that there are different mechanisms behind the structuring of particles in the flow which are not always well understood. The problem even increases in its complexity when considering soft particles. Flows in microfluidic devices are commonly believed to be in the fully viscous regime (Stokes limit). However, inertia can play a role if channel diameters are larger than $\approx 100 \mu\text{m}$ (Di Carlo 2009). Inertia effects may then be used to enhance mixing and to separate or focus particles in straight or curved geometries (Munn & Dupin 2008; Hur *et al.* 2011; Tanaka *et al.* 2012; Martel & Toner 2012).

The non-inertial lateral motion of single deformable particles (such as vesicles, capsules or red blood cells) in Poiseuille flow has been thoroughly studied over the past years (Doddi & Bagchi 2008*b*; Kaoui *et al.* 2008, 2009; Danker *et al.* 2009; Coupier *et al.* 2008; Shi *et al.* 2012). Only recently, the effect of inertia on the dynamics of deformable objects has been investigated systematically (Doddi & Bagchi 2008*a*; Nourbakhsh *et al.* 2011; Kilimnik *et al.* 2011; Shin & Sung 2011; Kim & Lai 2012; Shin & Sung 2012; Laadhari *et al.* 2012; Salac & Miksis 2012; Luo *et al.* 2013; Chen 2014). Almost all authors report an increase of particle deformation and inclination with Re . Additionally, Doddi & Bagchi (2008*a*) observed a change of the nature of hydrodynamic interactions of capsules upon an increase of the Reynolds number; the self-diffusive collision for small Re is replaced by spiralling motion. Furthermore, Laadhari *et al.* (2012) and Kim & Lai (2012) found that increasing fluid inertia shifts the tank-treading-to-tumbling transition of vesicles to larger values of the viscosity contrast. Shin & Sung (2011, 2012) demonstrated that the lateral equilibrium position of single capsules in 2D inertial channel flow has a maximum at about $Re = 50$.

In the present study, we investigate — *via* combined finite element, immersed boundary and lattice-Boltzmann simulations — the behaviour of a semi-dilute suspension ($\approx 10\%$ volume fraction) of deformable capsules in a confined channel. In contrast to previous studies, we consider a large range of channel Reynolds numbers between 3 and 417 and capillary numbers between 0.003 (nearly rigid) and 0.3 (strongly deformed). We investigate in detail the macroscopic and microscopic behaviour of the suspension as function of Re and Ca , such as global and local viscosity, concentration profiles, depletion layer thickness, particle deformation and inclination. We observe a strong inertial focusing at large Re and Ca ; particles tend to cluster in a narrow region about the centreplane, reducing the overall viscosity of the suspension. This effect is rationalised in terms of the behaviour of a single particle (dilute suspension limit) and hydrodynamic interactions between particles at finite volume fraction.

The article is structured as follows. Section 2 briefly describes the numerical model and introduces the simulation parameters. The numerical results are presented and discussed in section 3. Finally, the findings are summarised and conclusions are provided in section 4.

2. Computational method and simulation parameters

2.1. Computational model

We use the Bhatnagar-Gross-Krook (BGK) lattice-Boltzmann (LB) method with the D3Q19 velocity set (Succi 2001; Aidun & Clausen 2010; Krüger *et al.* 2011) to compute the fluid flow in the entire domain. The fluids inside and outside the capsules are modelled with the same density and viscosity. The kinematic viscosity ν is related to the BGK relaxation parameter τ according to

$$\nu = c_s^2 \left(\tau - \frac{1}{2} \right) \Delta t, \quad (2.1)$$

where Δt is the time step and c_s is the speed of sound. The lattice constant is denoted Δx . The no-slip boundaries at the channel walls are realised through the half-way bounce-back boundary condition (Ladd 1994). To include a body force we follow the Shan-Chen forcing approach (Shan & Doolen 1995).

Each capsule is described as a closed massless membrane discretised into a triangular mesh with 980 facets (Krüger *et al.* 2011). In the absence of external stresses the particles assume a spherical equilibrium shape with radius r . The in-plane energy of a particle membrane is given by the elastic law of Skalak *et al.* (1973):

$$E_s = \oint dA \left[\frac{\kappa_s}{12} (I_1^2 + 2I_1 - 2I_2) + \frac{\kappa_\alpha}{12} I_2^2 \right], \quad (2.2)$$

where κ_s is the shear elasticity and κ_α is the area dilation modulus and the integral runs over the entire capsule surface. The parameters I_1 and I_2 are the in-plane strain invariants which can be derived from the local membrane deformation tensor as detailed by Krüger *et al.* (2011). To avoid buckling (Kilimnik *et al.* 2011), the capsules also have a finite bending resistance with discretised bending energy

$$E_b = \frac{\sqrt{3}\kappa_b}{2} \sum_{\langle i,j \rangle} (\theta_{ij} - \theta_{ij}^{\text{eq}})^2. \quad (2.3)$$

This is a simplified version of the classical Helfrich form (Helfrich 1973). The bending modulus is denoted by κ_b , and the sum runs over all pairs of neighbouring facets (*i.e.*, facets with one common edge). Each facet pair has an equilibrium normal-to-normal angle

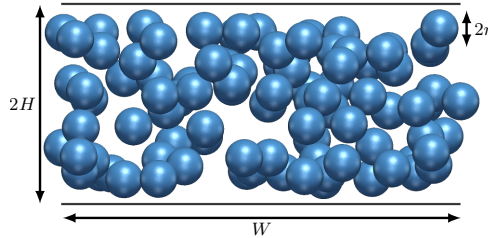


FIGURE 1. (Colour online) Geometrical setup. The distance between the confining walls is $2H$, and the length and width of the channel is W . The undeformed particle radius is r . The snapshot shows a random initial state.

θ_{ij}^{eq} defined by the initially spherical capsule shape. The elastic forces are computed *via* the principle of virtual work (Charrier *et al.* 1989; Krüger *et al.* 2011).

For the sake of simplicity and reduction of the parameter space dimensionality, the particle elasticities are fixed in a way such that the reduced area dilation modulus and reduced bending modulus,

$$\tilde{\kappa}_\alpha = \frac{\kappa_\alpha}{\kappa_s} = 2 \quad \text{and} \quad \tilde{\kappa}_b = \frac{\kappa_b}{\kappa_s r^2} = 2.87 \cdot 10^{-3}, \quad (2.4)$$

are constant. The typical maximum area extensions following from our choice of $\tilde{\kappa}_\alpha$ are $< 1\%$ for $Ca = 0.003$, $< 8\%$ for $Ca = 0.03$ and $< 20\%$ for $Ca = 0.3$. The above value for the bending resistance κ_b has been chosen for convenience. On the one hand, it is sufficiently small so that the elastic behaviour is dominated by the shear resistance. On the other hand, it is large enough to avoid buckling.

The immersed-boundary method (Peskin 2002) with a trilinear interpolation stencil as presented by Krüger *et al.* (2011) is used to couple the fluid flow and capsule dynamics. The system is assumed to be athermal, and thermal fluctuations are neglected. Therefore, all observed effects are flow-induced. We have implemented a soft repulsion force for particles near contact. This force becomes active when two mesh vertices of different particles come closer than one lattice constant. However, we observed that this force is rarely required since the volume fraction is rather small and the hydrodynamic interactions are usually sufficient to repel particles at small distances.

2.2. Simulation parameters and setup

We investigate the suspension rheology in a channel with width W between two planar walls at $z = \pm H$ ($2H$ is the distance between the walls) as illustrated in figure 1. The system is periodic along the x - and y -axes. Flow is induced by a constant body force density f along the x -axis. This geometry has been chosen for convenience; especially the data evaluation is facilitated by a planar rather than by a cylindrical or even a duct-like geometry.

Relevant simulation parameters are the volume fraction $\phi = 4\pi N r^3 / 3V$ (which is computed from the number N of particles, their initial, undeformed radius r , and the total system volume V) and the confinement $\chi = r/H$.

In order to control the Reynolds and capillary numbers independently, three simulation parameters are available: the kinematic viscosity ν of the ambient fluid, the external force density f , and the particle shear modulus κ_s .

We define the bare Reynolds number as

$$Re_0 = \frac{\hat{u}_0 H}{\nu} = \frac{f H^3}{2\rho\nu^2}, \quad (2.5)$$

where \hat{u}_0 is the centreplane velocity of the unperturbed flow (*i.e.*, without particles) and ρ is the fluid density. The solution for the unperturbed profile ($z = 0$ corresponds to the centreplane) is

$$u_0(z) = \hat{u}_0 \left[1 - \left(\frac{z}{H} \right)^2 \right], \quad \hat{u}_0 = \frac{fH^2}{2\rho\nu}. \quad (2.6)$$

The other important parameter is the shear capillary number as ratio of a typical shear stress magnitude $\bar{\sigma}$ to the characteristic elastic particle stress κ_s/r :

$$Ca = \frac{\bar{\sigma}r}{\kappa_s}. \quad (2.7)$$

We define the characteristic shear stress $\bar{\sigma}$ as the average shear stress in the system. For the unperturbed flow, the momentum balance requires the local condition

$$\sigma(z) = -fz. \quad (2.8)$$

This leads to the average stress magnitude

$$\bar{\sigma} := \frac{1}{2H} \int_{-H}^{+H} |\sigma(z)| = \frac{fH}{2}. \quad (2.9)$$

Equation (2.8) and (2.9) are also valid for flows perturbed by particles, as long as the suspension is in a quasi-steady (*i.e.*, on average non-accelerated) state and the stress is averaged over a sufficiently long time.

For the current study, the parameters $2H = 60\Delta x$ and $r = 5.9\Delta x$ have been chosen, and the particle number is $N = 96$ for the suspension and $N = 1$ for the single-particle reference simulations. The system size along the x - and y -axes is $W = 4H = 120\Delta x$ each, thus $\chi = 0.20$ is fixed and $\phi \approx 0.1$ for the suspension and $\phi \approx 0.001$ for the single particle. Since our primary interest is not on the effect of the confinement, we choose a moderate value, avoiding both highly and weakly confined situations.

The Reynolds and capillary numbers are varied in the intervals $[3, 417]$ and $[0.003, 0.3]$, respectively (corresponding to BGK relaxation parameters $\tau \in [0.5072, 1.4]$). Particles with $Ca = 0.003$ are nearly rigid, and a further decrease of Ca leads to stability problems. Capillary numbers larger than 0.3 are problematic because the capsule deformation becomes so severe that a higher resolution would be required to capture the local curvature. Without increasing the resolution the Reynolds number cannot be chosen smaller than 3 or much larger than 400 due to stability and accuracy considerations.

Since there is one degree of freedom left (three control parameters to set two target parameters), we choose the parameters in a way such that the unperturbed lattice centreplane velocity \hat{u}_0 in equation (2.6) is $\frac{1}{30} \frac{\Delta x}{\Delta t}$. This ensures a) small Mach numbers and therefore negligible compressibility artefacts and b) a sufficiently small time step to reduce time discretisation errors.

On the one hand, for a fixed capillary number, the Reynolds number is changed by adapting the kinematic viscosity ν in a way such that \hat{u}_0 in equation (2.6) remains constant. This requires a change of the force density $f \propto \nu$ which in turn leads to a change of $\kappa_s \propto f$ so that Ca remains constant as can be inferred from equation (2.7). On the other hand, Ca can be changed for constant Re just by adapting κ_s . Concluding, the relevant simulation parameters can be directly obtained from the target capillary and Reynolds numbers:

$$\nu = \frac{\hat{u}_0 H}{Re_0}, \quad f = \frac{2\rho\hat{u}_0}{Re_0 H}, \quad \kappa_s = \frac{\rho\hat{u}_0 r}{Ca Re_0}, \quad \kappa_\alpha = 2\kappa_s, \quad \kappa_b = 2.87 \cdot 10^{-3} \kappa_s r^2, \quad (2.10)$$

where $H = 60$, $r = 5.9$, $\hat{u}_0 = 1/30$ and $\rho = 1$ in simulation units ($\Delta x = \Delta t = 1$).

We stress that, in the present work, we focus on artificial capsules for which the selected ratio of Ca and Re_p (where $Re_p = \dot{\gamma}r^2/\nu$ is the Reynolds number on the particle scale) can be tuned. For example, healthy red blood cells (RBCs) in an aqueous environment have a fixed ratio $Ca/Re_p = \rho\nu^2/(\kappa_s r) \approx 50$. Investigating inertial effects on the scale of a single RBC would require $Re_p > 1$ and therefore $Ca > 50$ or, in physical units, $\dot{\gamma} > 6 \cdot 10^4/\text{s}$. For RBCs, it is therefore impossible to achieve high Re_p and small Ca at the same time. Contrarily, by changing r and κ_s of artificial capsules, the ratio Ca/Re_p can be controlled.

As initial condition, the undeformed spherical particles in the suspension with $\phi = 0.1$ were randomly distributed in the fluid volume avoiding overlap with each other and the walls. The single particle was released half-way between the centreplane and one of the walls, but reference simulations with different initial positions gave the same final state. The initial fluid density was unity everywhere, and the flow profile was fully developed according to equation (2.6). Starting with a fully developed velocity profile is necessary to avoid long transients. The time scale for acceleration of the entire fluid from a quiescent to a fully developed state is proportional to the momentum diffusion time $t_{\text{md}} \sim H^2/\nu$. Especially for high Reynolds numbers, when the kinematic viscosity ν is small, t_{md} becomes undesirably large.

All suspension simulations ran for $6 \cdot 10^5$ time steps which turned out to be sufficient to obtain converged particle concentration profiles. During this time, a particle at the centreplane is advected by a distance equal to about 3400 particle radii. We define the Stokes time as the time a particle at the centreplane would require to travel its own radius. Here, the Stokes time corresponds to 177 time steps. We made sure that all single particle simulations ran until the particle reached its lateral equilibrium position. As a rule of thumb, the required number of time steps decreased with Re , and the characteristic time scale for lateral migration was found to be between 50 and 1100 Stokes times.

3. Results and discussion

We restrict ourselves to the quasi-steady-state properties of the suspensions. Hur *et al.* (2010) provided an estimate for the channel length required for inertial particle focusing:

$$\frac{L_f}{r} = \frac{\pi}{f_L \chi^3 Re_0} \sim \frac{\mathcal{O}(10^4)}{Re_0}, \quad (3.1)$$

where f_L is a geometry-dependent parameter on the order of 0.03 and the confinement $\chi = r/H \approx 0.2$ has been used. We therefore expect a slower convergence to a steady state for smaller Re_0 . In particular, for $Re_0 = 6$ we predict $L_f/r \sim \mathcal{O}(2000)$. Indeed, our simulation results for the suspensions show that a quasi-steady state is reached after about 1000–1500 Stokes times ($\approx 1.8 \cdot 10^5$ – $2.7 \cdot 10^5$ time steps), depending on the values of Re_0 and Ca . Therefore, we drop the initial 1700 Stokes times ($3 \cdot 10^5$ time steps) in all data sets and report only results obtained afterwards. Observables are instantaneously averaged over the periodic x - and y -directions and shown as functions of the transverse coordinate z only. Any reported errors correspond to the variance due to collision-induced fluctuations about the time average. We note that the effect of the volume fraction on the convergence time is itself an interesting problem which, however, is not within the scope of the present work.

We discuss the apparent suspension viscosity in section 3.1 before turning our attention to the lateral particle distribution (section 3.2). Based on these findings, we first come back to the local suspension rheology in section 3.3 before we describe the results obtained

for a single particle in section 3.4. The particle properties, such as deformation and inclination, are investigated in section 3.5.

3.1. Apparent suspension viscosity

The volume flux of a simple fluid along the x -axis with viscosity η_0 through a channel segment with width W reads

$$Q_0 = \int_0^W dy \int_{-H}^{+H} dz u_0(z) = \frac{2fH^3W}{3\eta_0}, \quad (3.2)$$

where the velocity $u_0(z)$ is given by equation (2.6). For a complex fluid, like a suspension, the viscosity is generally not uniquely determined in such a flow geometry, but one can use equation (3.2) to define an effective viscosity if the flux Q is known:

$$\eta := \frac{2fH^3W}{3Q}. \quad (3.3)$$

The reduced apparent viscosity is the dimensionless ratio

$$\eta_a = \frac{\eta}{\eta_0}. \quad (3.4)$$

For the sake of convenience, we denote η_a simply as *viscosity* if not clearly specified otherwise. In terms of the unperturbed (particle-free) flux Q_0 and the measured flux Q , the viscosity is $\eta_a = Q_0/Q$ and typically larger than unity.

For an observer who is not aware of the microstructure of the suspension, the presence of the particles has one major effect; the volume flux is reduced by a factor η_a , and the viscosity is accordingly increased by the same factor. This means that the *apparent* Reynolds number (defined by the *apparent* viscosity and measured flow rate) is decreased by a factor η_a^2 . It is therefore convenient to use $Re = Re_0/\eta_a^2 < Re_0$ as the appropriate Reynolds number for the macroscopic suspension. One should keep in mind that Re , contrarily to Re_0 , is not known *a priori*.

Figure 2 shows the viscosity η_a of the suspension with $\phi = 0.1$ as function of Re for all considered capillary numbers. One observes that, for a given value of Re , suspensions of softer particles always appear less viscous than suspensions of more rigid particles. This is a well-known behaviour of deformable particle suspensions (Bagchi & Kalluri 2010). Soft particles adapt more easily to the flow field and disturb it less. The particles in the small Ca regime give rise to a monotonically increasing viscosity as function of Re . However, at $Ca \geq 0.03$, the suspension shows an interesting behaviour; after an initial viscosity increase up to $Re \approx 45$, the viscosity decreases again. We will explain this effect by taking into account the observed lateral particle distributions and the local rheology (section 3.2 and 3.3). As a remark, we expect that, in the Stokes limit ($Re \rightarrow 0$), the viscosity reaches a Re -independent plateau whose height depends only on Ca .

3.2. Lateral particle distribution and inertial focusing

In order to quantify the microscopic structure of the suspension, we first focus on the lateral distribution of the particles. Let $\phi(z)$ be the volume fraction (or particle concentration) profile between the channel walls. We define the second moment of the particle density as a measure for the lateral distribution of the particles:

$$M_2 := \frac{1}{2H} \int_{-H}^{+H} \phi(z) z^2 dz. \quad (3.5)$$

In order to take advantage of this quantity, we introduce the lateral displacement parameter Δ as the square root of the normalised second moment ($\Delta \propto \sqrt{M_2}$) such that

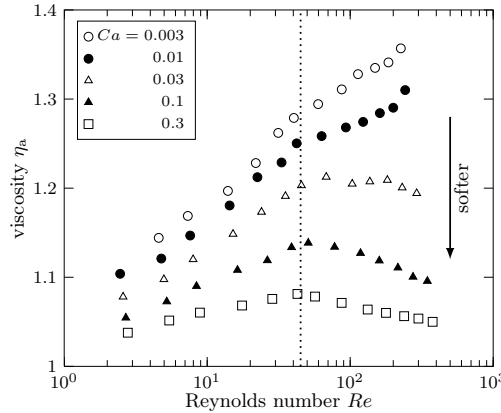


FIGURE 2. Viscosity η_a (equation (3.4)) as function of Reynolds number Re for different values of the capillary number Ca for $\phi = 0.1$. Error bars are of the order of the symbol size. While the suspension exhibits a monotonic increase of η_a for more rigid particles (small Ca), the viscosity decreases for strongly deformable particles (large Ca) for $Re > 45$ (dotted line). Softer particle suspensions always appear less viscous for fixed Re .

a delta distribution $\phi(z) = 2H\phi\delta(z - z_p)$ yields $\Delta = \pm|z_p|/H$. This way, Δ equals the non-dimensional lateral position of a small single particle in the channel (with possible values in the interval $[-1, +1]$). For a delta-distribution located at z_p we find

$$M_2 = \frac{1}{2H} \int_{-H}^H 2H\phi\delta(z - z_p)z^2 dz = \phi z_p^2 \quad (3.6)$$

and therefore

$$\Delta = \sqrt{\frac{M_2}{\phi H^2}}. \quad (3.7)$$

The parameter Δ can be considered as the average dimensionless lateral position of the particles. A perfectly homogeneous suspension yields $\Delta = \sqrt{1/3}$. Additionally to Δ , we define the reduced instantaneous depletion layer thickness d as the minimum distance of any particle's surface element to any confining wall, normalised by H .

The lateral displacement parameter Δ as function of Re is shown for different Ca in figure 3a. Softer particles are always more strongly concentrated near the centreplane for fixed Re . For all values of Ca , Δ has a maximum in the vicinity of $Re = 45$. Except for their magnitude, the shapes of the Δ -curves are rather similar for different capillary numbers. Interestingly, Shin & Sung (2011) also noticed a maximum lateral displacement of a single 2D elastic capsule in inertial flow for $Re = 30$ in a channel with a confinement of 0.1.

Figure 3b contains the data for the depletion layer thickness d . More rigid particles tend to be closer to the confining walls for increasing Re . For the stiffest particles ($Ca = 0.003$), the depletion layer thickness at small Re is about 10% of the channel half-width, and it decreases to about 5% for the largest simulated Reynolds number. Already for $Ca = 0.03$, but especially for even larger Ca , the function $d(Re)$ has a minimum. For $Ca = 0.3$, d is almost constant up to $Re \approx 40$. Beyond, the depletion layer significantly increases and reaches values of nearly 50% for $Re = 417$. The particles are strongly focused towards the centreplane upon increasing Re ; we therefore call this effect *inertial focusing*. It should be noted that this term has been used by other authors to describe different effects (Di Carlo 2009; Humphry *et al.* 2010; Martel & Toner 2012). By comparing figure 2 and figure 3b,

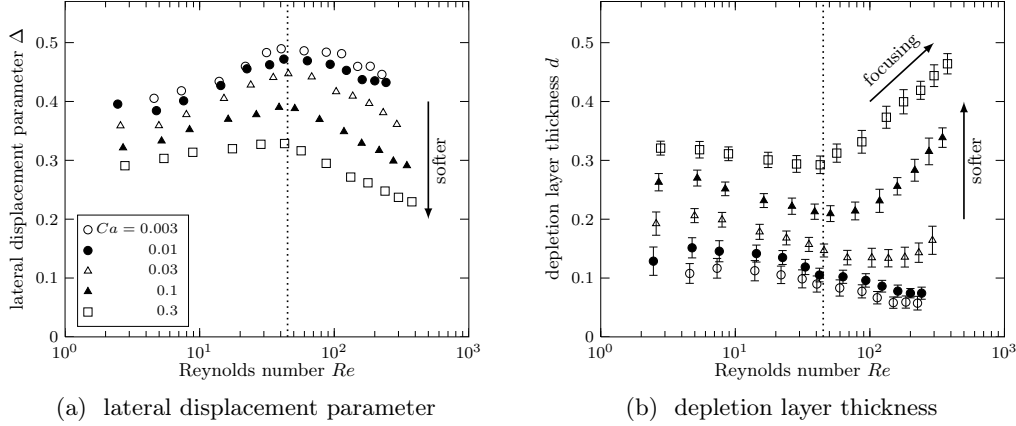


FIGURE 3. Characterisation of the lateral particle distribution for $\phi = 0.1$. (a) Lateral displacement parameter Δ (equation (3.7)). Errors are of the order of the symbol size. A perfectly homogeneous suspension corresponds to a value of $1/\sqrt{3} \approx 0.57$ (top edge). Smaller values indicate a concentration of particles closer to the centreplane. On average, softer particles (larger Ca) are always closer to the centreplane for a given Re . Note the presence of a maximum for each curve at $Re \approx 45$ (dotted line). Beyond this value, particles tend to move closer to the centreplane again. (b) Reduced depletion layer thickness d . For $d = 0$, particles would touch the walls; $d = 1$ corresponds to the centreplane. The legend is valid for both plots. The effect of inertia is almost negligible for $Re < 10$. More rigid particles (smaller Ca) tend to form the thinnest depletion layer. Deformable particles show a strongly Re -dependent behaviour; for $Re > 45$ (dotted line), the depletion layer grows significantly.

we also observe that the thickness of the depletion layer and the suspension viscosity are tightly connected. The viscosity increases when the depletion layer thickness decreases and vice versa. A large depletion layer thickness d reduces the viscous dissipation in wall vicinity. This is related to the Fåhræus-Lindqvist effect (Fåhræus & Lindqvist 1931) observed in blood flow; however, in the present case, the depletion layer thickness is controlled by the Reynolds number and not the degree of confinement of red blood cells in a vessel.

Interestingly, the peak in $\Delta(Re)$ and the increase of the depletion layer $d(Re)$ for large Ca (figure 3) are observed at a similar Reynolds number (≈ 45) where also the kink in the apparent viscosity $\eta_a(Re)$ in figure 2 is located. This suggests a strong dependence of the viscosity on the particle distribution. We will come back to this observation in section 3.3. Similarly to the data in figure 2 it is expected that all curves in figure 3 reach a Ca -dependent plateau for $Re \rightarrow 0$.

Due to the non-homogeneous stress and particle density distributions it is difficult to achieve data collapse in figure 3 and to find simple, globally defined scaling laws.

Some characteristic particle configurations and density profiles $\phi(z)$ are shown in figure 4. In the limit of small Reynolds and capillary numbers ($Re_0 = 6$ and $Ca = 0.003$), the particles are basically undeformed and unevenly distributed throughout the channel. By increasing their deformability ($Ca = 0.3$), the particles move closer towards the centreplane. At the intermediate Reynolds number $Re_0 = 50$ the nearly rigid particles ($Ca = 0.003$) show an affinity for distances half-way between the centreplane and the walls which reminds of a Segré-Silberberg-like behaviour (Segré & Silberberg 1962*a,b*). This effect disappears for $Ca = 0.3$ where configuration and particle distribution look very similarly to that at $Re_0 = 6$ and $Ca = 0.3$. We therefore conclude that the Segré-Silberberg effect can be suppressed by choosing sufficiently soft particles.

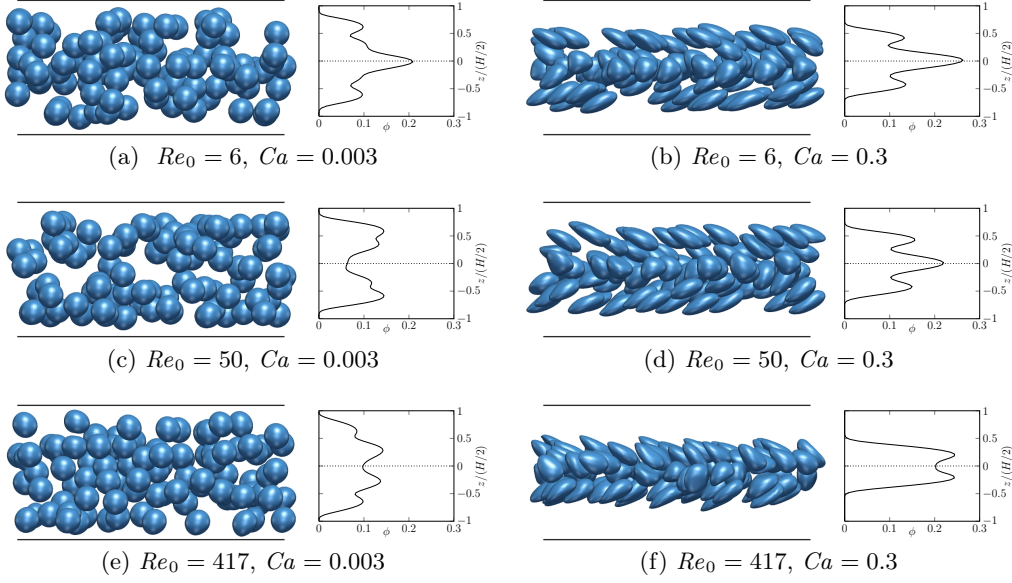


FIGURE 4. (Colour online) Exemplary instantaneous quasi-steady-state configurations of the particles (snapshots) and corresponding time-averaged particle concentration profiles (plots) for different combinations of Reynolds and capillary numbers. The dotted lines correspond to the centreplane. (a) For $Re_0 = 6$ and $Ca = 0.003$ neither inertial nor deformability effects are very important. (b) Increasing the capillary number to 0.3 leads to a migration of the particles towards the centreplane. (c) For $Re_0 = 50$ and $Ca = 0.003$ the nearly rigid particles are pushed towards the walls and prefer lateral positions resembling the Segré-Silberberg effect. (d) This behaviour is distorted when the particles are strongly deformable ($Ca = 0.3$), and the concentration profile is rather similar to that for smaller Re_0 in (b). (e) For large Reynolds numbers ($Re_0 = 417$) the Segré-Silberberg-like behaviour of the nearly rigid particles ($Ca = 0.003$) is less pronounced, and the particles are closer to the centreplane on average. (f) When both inertial effects and deformability are important ($Re_0 = 417$, $Ca = 0.300$), the particles are strongly focused and concentrated in the central region.

For even larger Re_0 ($Re_0 = 417$) the more rigid particles are more homogeneously distributed, but they show a strong inertial focusing when both Re and Ca are large. In the latter case, the depletion layer is very pronounced and the average particle concentration near the centreplane is greater than 20% and therefore more than twice as large as the overall average. In all cases, several individual density peaks are visible. These are probably due to the relatively large confinement ($\chi = 0.2$) (Li & Pozrikidis 2000; Zurita-Gotor *et al.* 2012).

Before we turn our attention more closely to the mechanisms responsible for the lateral particle distribution in section 3.4, let us first discuss the local suspension rheology.

3.3. Local rheology and dependence of viscosity on suspension microstructure

In order to quantify the *local* rheology, we define the reduced local viscosity η_{loc} in a plane at a given z -value as the ratio of the known stress at position z (equation (2.8)) divided by the measured average shear rate $\dot{\gamma}(z)$ in this plane:

$$\eta_{\text{loc}}(z) := \frac{1}{\eta_0} \frac{\sigma(z)}{\dot{\gamma}(z)}. \quad (3.8)$$

Figure 5 shows the dependence of η_{loc} on the local volume fraction for a few selected parameter sets for $Ca = 0.03$ (similar results have been obtained for the other capillary

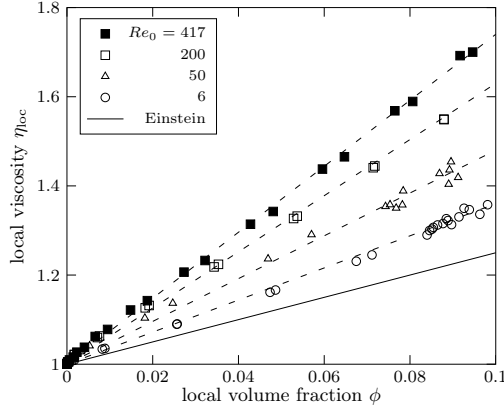


FIGURE 5. The local viscosity is shown as function of the local volume fraction for $Ca = 0.03$ and a few Reynolds numbers. The viscosity is a monotonically increasing function of both the volume fraction ϕ and the Reynolds number Re . For the sake of comparison, we also show Einstein's viscosity $(1 + \frac{5}{2}\phi)$ one would expect for a dilute suspension of rigid spheres in a simple viscous shear flow. The local viscosity is roughly linear in ϕ as indicated by the dashed lines as guide for the eyes.

numbers). We construct these data sets from a combination of $\phi(z)$ (figure 4) and $\eta_{loc}(z)$ (not shown). All data in the central region ($|z/r| < 1$) are excluded due to large fluctuations; both the stress and the shear rate are small for $z \rightarrow 0$, and their ratio is prone to significant noise.

As expected, the local viscosity is a monotonically increasing function of the local volume fraction for all investigated data sets. The ϕ -dependence is roughly linear up to $\phi = 0.1$. Furthermore, local viscosities in our simulations are generally decreasing with Ca as the particles become softer and contribute less to dissipation (data not shown).

We also notice that η_{loc} is strictly increasing with Re for fixed ϕ . This behaviour will be explained based on the particle properties in section 3.5. The viscosity curves $\eta_{loc}(\phi)$ shown in figure 5 are larger than the corresponding Einstein viscosity $(1 + \frac{5}{2}\phi)$ of a dilute suspension of hard spheres with negligible inertia. It is not clear how $\eta_{loc}(\phi)$ behaves for $Re \rightarrow 0$ since this parameter region is not accessible in the current simulation setup.

We can now turn our attention back to the apparent viscosity η_a (section 3.1). There are two mechanisms which lead to a variation of $\eta_a(Re)$.

(a) For a fixed density distribution $\phi(z)$, the viscosity η_a is expected to grow with Re because η_{loc} increases with Re (figure 5).

(b) A Re -induced redistribution of particles towards the centreplane tends to reduce η_a because less particles are located in high-dissipation regions. Viscous dissipation generally scales like the product of shear rate $\dot{\gamma}$ and fluid shear stress σ_f . As a consequence, most of the dissipation in a Poiseuille-like flow occurs in the wall region where $\dot{\gamma}$ and σ_f are large. Therefore, η_a is dominated by the contribution of η_{loc} in wall vicinity, whereas η_{loc} in the central region is less relevant.

The first effect can be seen for suspensions with $Ca = 0.003$ and 0.01 ; figure 3 reveals that the lateral particle distribution changes only slightly with Re for $Re > 45$. Yet, η_a shows a strong increase (figure 2), which can be attributed to the increase of η_{loc} with Re . The second effect is particularly important for $Ca = 0.1$ and 0.3 ; the increase of η_{loc} with Re is overcompensated by the strong focusing of particles (figure 3), and η_a decreases (figure 2). This can also be seen in figure 6 where a few selected velocity profiles for $Ca = 0.3$ are shown. For $Re > 45$, particles are more concentrated near the

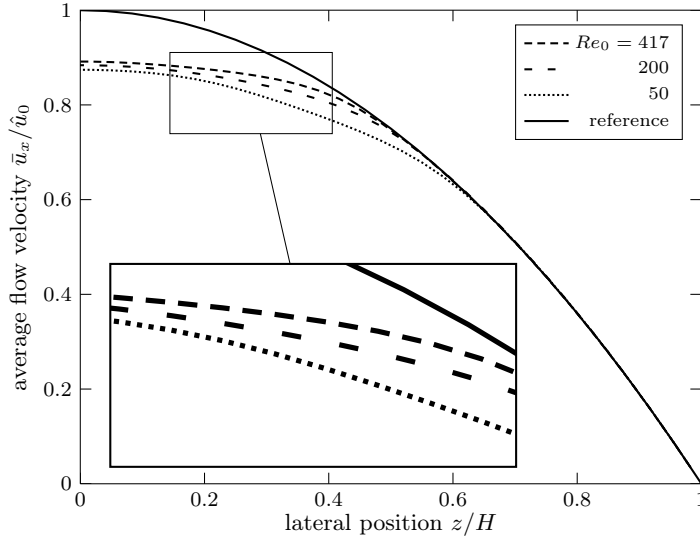


FIGURE 6. Representative averaged velocity profiles $\bar{u}_x(z)$ for $Ca = 0.3$ and $\phi = 0.1$. The reference profile equation (2.6) without particles is shown as solid line. For $Re = 417$, the area below the curve (*i.e.*, the total flux) is larger than for $Re = 50$ or 200 .

centreplane, and the velocity profiles approach the reference profile without particles. This results in a larger flux Q , and η_a decreases. For $Ca = 0.03$, both above-mentioned effects basically compensate each other, and η_a remains roughly constant for $Re > 45$ (figure 2). In general, the velocity profiles in figure 6 show a pronounced flattening near the centreplane which is typical for shear-thinning fluids.

Concluding we note that, although the suspensions investigated here show a strict increase of $\eta_{loc}(Re)$ when observed locally, η_a can decrease since the particles are inhomogeneously distributed throughout the channel and this microstructure changes with Re . Such an effect would therefore not be observed in an unbounded simple shear flow where the stress and dissipation are homogeneous on average.

3.4. Mechanisms responsible for lateral particle distribution

In a steady state, the lateral position of particles (either isolated or in a denser suspension) is the consequence of the balance of forces pointing towards and away from the centreplane. For rigid particles at intermediate Reynolds numbers, the inertial lift is balanced by the wall repulsion, which gives rise to the Segré-Silberberg effect. Deformable particles tend to approach the centreplane due to a combination of wall repulsion and deformability in the presence of a curved velocity profile (Kaoui *et al.* 2009). This effect may be partially compensated by an inertial lift force if the Reynolds number is sufficiently large. In a non-dilute suspension, not all particles can be located at the centreplane at the same time. Hydrodynamic interactions usually lead to non-reversible particle trajectories and a diffusive motion (Eckstein *et al.* 1977; Pranay *et al.* 2012) which result in a wide distribution of particles across the channel. However, Doddi & Bagchi (2008a) reported that the nature of the hydrodynamic interactions of deformable capsules changes in the presence of inertia. The diffusive motion of two colliding capsules in shear flow can be replaced by spiralling motion at larger Re . In a suspension of sufficiently soft particles, this may lead to a reduced hydrodynamic repulsion and therefore to a larger concentration near the centreplane as we observe it in figure 3 and 4.

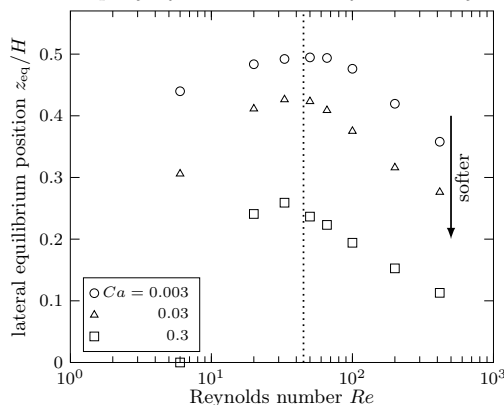


FIGURE 7. Lateral equilibrium position z_{eq} of a single capsule ($N = 1$, $\phi = 0.001$) as function of Re for different values of Ca . Note the data point $z_{eq} = 0$ for $Re = 6$ and $Ca = 0.3$. The vertical dotted line marks $Re = 45$ (cf. figure 3).

Therefore, we have investigated two distinct ingredients responsible for the final lateral distribution of the suspended particles:

- What is the lateral equilibrium position of a single particle ($\phi \rightarrow 0$)?
- How do particle-particle collisions in the suspension ($\phi = 0.1$) contribute?

Figure 7 shows the lateral equilibrium position z_{eq} of a single capsule ($N = 1$, $\phi = 0.001$) in an otherwise identical environment as the suspension with $\phi = 0.1$. The similarity to the lateral displacement parameter Δ in figure 3a is striking. In particular, the curves $z_{eq}(Re)$ for different Ca feature a peak near $Re = 45$ at which the particle is closest to one of the walls. This leads to the assumption that the overall behaviour of the lateral particle distribution in the suspension, and therefore the inertial focusing, is strongly determined by that of a single particle. We note that for $Re \rightarrow 0$, the capsule should eventually reach the centreplane for any finite value of Ca . Therefore, inertia is responsible for the finite values of z_{eq} . However, for increasing Ca , the deformability effect becomes more important and the capsule reaches a configuration closer to the centreplane. Interestingly, we observe only the capsule for $Re = 6$ and $Ca = 0.3$ reaching the centreplane. For this particular data point, deformability effects are strongest and inertia effects are weakest. Shin & Sung (2011) observed a similar variation of $z_{eq}(Re)$ for simulated deformable capsules in 2D. In particular, for a confinement of $\chi = 0.2$, they observed the maximum of $z_{eq}(Re)$ between $Re = 30$ and 40 , depending on the details of the particle deformability (note that their definition of Re is identical to ours).

The lateral particle distributions as shown in figure 3 and 4 are not only a result of the single particle behaviour in figure 7. If this was the case, one would find all particles located on two planes corresponding to $\pm z_{eq}$. This is obviously not the case, so particle-particle interactions play an important role as well. For example, we find $z_{eq}(Re = 417)/H = 0.36$, 0.28 and 0.11 for $Ca = 0.003$, 0.03 and 0.3 , respectively, but $\Delta = 0.45$, 0.36 , 0.23 for the suspension for the same values of Re and Ca . Particle-particle interactions therefore lead to a *dispersion* of the particles, pushing them farther towards the walls. Figure 8 shows the average of the magnitude of the lateral particle velocity, $\overline{|u_z|}/\hat{u}_0$, which is an indicator for lateral particle dispersion. We observe that the fluctuation profile for $Ca = 0.03$ does not strongly depend on the Reynolds number (figure 8a). However, a combination of large Ca and Re leads to a dramatic decrease of the lateral particle motion (figure 8b) which could be related to the effect described by

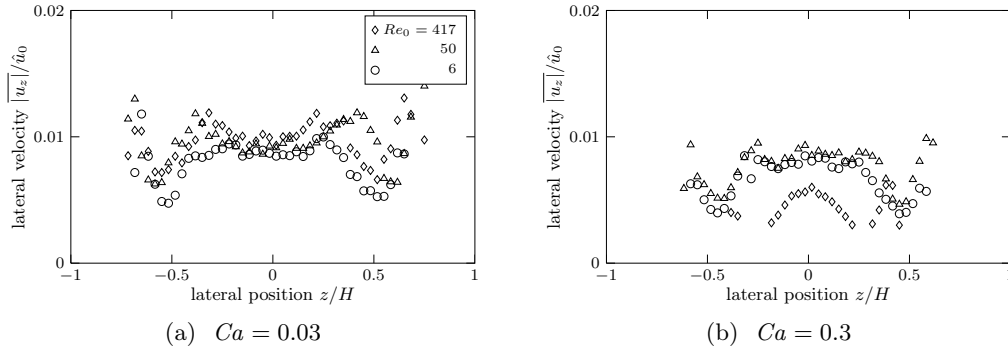


FIGURE 8. Average of the lateral particle velocity magnitude $|u_z|$ normalised by the reference velocity \hat{u}_0 for (a) $Ca = 0.03$ and (b) $Ca = 0.3$. The legend is valid for both plots. Particular attention should be paid to the fluctuations for $Re_0 = 417$ and $Ca = 0.3$ (\diamond in (b)): Velocity fluctuations are significantly smaller than for smaller values of Re_0 at the same Ca , which is not observed for $Ca = 0.03$. This suggests that the combination of large Re and Ca reduces the particle dispersion which facilitates particle focusing.

Doddi & Bagchi (2008a) and further facilitates inward migration and therefore particle focusing.

In the present case, it is expected that (i) the wall repulsion, (ii) the particle deformation in the presence of a curved velocity profile, (iii) the inertial lift and (iv) the hydrodynamic dispersion of particles all play a role. These contributions are generally different functions of Ca and Re and also of volume fraction and confinement.

3.5. Particle properties

After having presented the suspension properties, let us turn to the behaviour of the suspended particles. All particles have been observed to perform tank-treading-like dynamics at all times. This is in agreement with previous investigations of initially spherical capsules (Yazdani *et al.* 2011). We note that initially non-spherical capsules can also undergo tumbling motion (Shin & Sung 2012). Only the single particle on the centreplane ($Re = 6$, $Ca = 0.3$) does not perform tank-treading, but rather assumes a steady bullet-shape configuration. In the suspension, deformations and inclinations are fluctuating due to particle-particle interactions.

The particle deformation is quantified by the Taylor deformation parameter

$$D = \frac{a - c}{a + c} \geq 0 \quad (3.9)$$

where a and c are the largest and smallest axes of the inertia ellipsoid of the deformed particle (Krüger *et al.* 2011). Undeformed particles fulfil $a = c$ and therefore $D = 0$. The deformation is related to the constitutive law of the particles and the fluid stresses on the particle surface which are responsible for their deformation. Based on the analytical work by Barthès-Biesel & Rallison (1981), one can compute the deformation parameter of a capsule in simple shear flow for a given capillary number in the small deformation regime (*i.e.* for particle shapes with a small deviation from that of a sphere). We consider deformations large if $D > 0.1$ (corresponding to an aspect ratio of $a/c > 1.22$). For the elasticity model employed in the current work, the relation between the deformation

parameter and the capillary number reads

$$D = \frac{45}{4} \frac{\frac{\kappa_\alpha}{\kappa_s} + \frac{2}{3}}{2 \frac{\kappa_\alpha}{\kappa_s} + 1} Ca \quad (3.10)$$

up to first order in Ca . As $\kappa_\alpha/\kappa_s = 2$ is fixed in the present study, one predicts $D = 6 Ca$ in the small deformation limit. It has to be noted that equation (3.10) is only valid for $\kappa_b = 0$ which is not the case in our simulations. However, as κ_b is rather small, it is expected that the bending elasticity becomes only important when the local membrane curvature is large. Due to equation (2.8) the shear stress, and therefore the local capillary number, increases with distance from the centreplane (*i.e.*, $Ca = Ca(z)$), and the particle deformation is an increasing function of the lateral particle position z .

The time-averaged particle deformation parameter $D(z)$ is presented in the left column of figure 9 together with the data points for a single particle in its final equilibrium state. Equation (3.10) is shown in the plots as a solid black line. For the smallest capillary number ($Ca = 0.003$), all particles are only slightly deformed. The deformations at $Re = 6$ match the theory for single capsules in simple shear flow except for particles which are closest to the walls. The reason is that the flow is inhomogeneous and the particles are extended. The outermost particles are in very close proximity to the walls (figure 4a); this leads to an additional particle deformation. We emphasise that the small deformation theory is only strictly valid for single isolated particles in simple shear flow. Still, it provides a good approximation in the present case.

For $Ca = 0.03$, where the deformation is larger and therefore less well described by the linear relation in equation (3.10), we observe that particle deformation increases with the Reynolds number. A similar trend has been observed for simulated three-dimensional capsules (Doddi & Bagchi 2008a) and two-dimensional vesicles (Kim & Lai 2012; Laadhari *et al.* 2012). This can be understood by considering the local particle reference frame; for a tank-treading capsule or vesicle, the fluid circulates around the particle. The curvature radius of the streamlines is smallest near the particle tips so that inertia leads to larger centrifugal drag forces at the tips and therefore to a larger deformation. The observed increase of deformation with Re is expected to amplify the inward migration of the particles, which may at least partially explain the data in figure 7 and therefore the inertial focusing in figure 3 and 4.

For an even higher capillary number ($Ca = 0.3$) the deformation is very large, reaching aspect ratios of more than $a/c = 2.5$. The theory by Barthès-Biesel & Rallison (1981) is not valid anymore. Interestingly, the Re -dependence nearly vanishes then; only in the central region ($z \approx 0$) the deformation increases with Re . The particles are probably already deformed so much that the additional inertial stresses do not contribute noticeably. It is interesting to note that also particles at the centreplane are deformed, which is caused by their finite size.

The inclination angle of a particle is the angle between its large main axis and the flow direction. In the small deformation regime the inclination angle assumes a value

$$\frac{\theta}{2\pi} = \frac{\theta_0}{2\pi} - \frac{15}{16} Ca \quad (3.11)$$

where $\theta_0 = \pi/4$ (*i.e.*, 45°) is the asymptotic value for $Ca \rightarrow 0$ (Barthès-Biesel 1980). The computed inclinations are shown in the right column of figure 9 for three different capillary numbers. Since the angles for $z < 0$ are negative, we report only the magnitude and denote it by θ . Indeed, figure 9 reveals that all particles at $|z| > r$ have an inclination angle of $\approx 45^\circ$ in the limit of small Re and Ca . Depending on Ca , one observes different characteristics of the inclination angle. For $Ca = 0.003$, θ strongly depends on

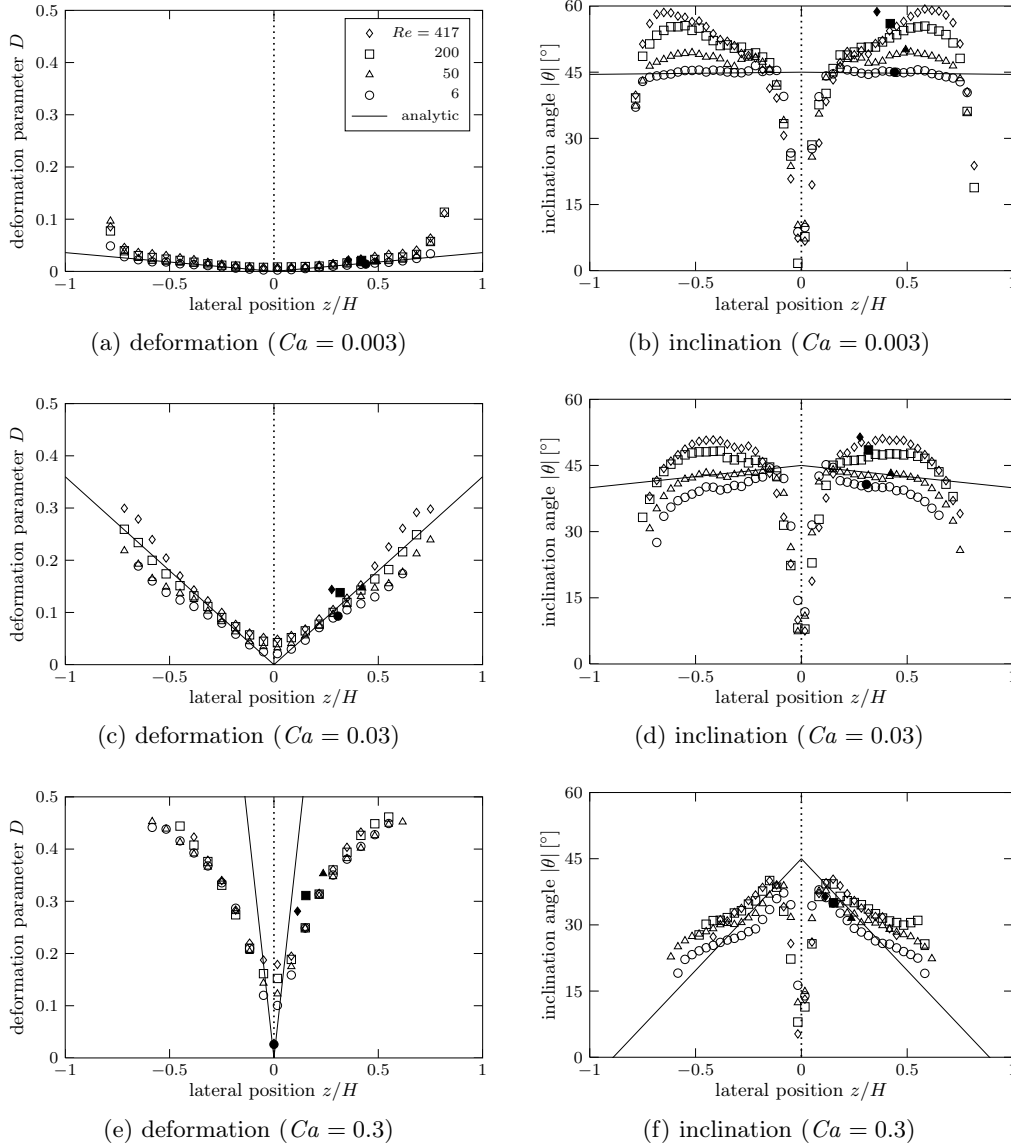


FIGURE 9. Deformation parameter D (left column) and inclination angle θ (right column) for different Re and (a), (b) $Ca = 0.003$, (c), (d) $Ca = 0.03$ and (e), (f) $Ca = 0.3$. The legend is valid for all plots. For the suspension (open symbols), only every second data point of D is shown for the sake of clarity. Filled symbols denote the data points for a single particle. The vertical dotted line corresponds to the centreplane. The inclined solid lines correspond to the small deformation predictions (equation (3.10) (Barthès-Biesel & Rallison 1981) and (3.11) (Barthès-Biesel 1980), respectively). The small deformation theory predicts the results for small Ca and Re well. Inertia effects tend to increase the particle deformation and inclination.

Re , especially in the wall vicinity. However, θ increases with Re and reaches values of about 60° . Laadhari *et al.* (2012) also observed an increase of the inclination angle of steadily tank-treading vesicles with Re . Only in the vicinity of the centreplane ($|z| < r$), θ is independent of Re . Also for $Ca = 0.03$ and 0.3 , the angles are strictly increasing with Re . The increase of the local viscosity with Re (figure 5) can be explained based on

these findings; when the average inclination angle increases with Re , the particles assume a larger cross-section in the channel, which in turn leads to a larger flow resistance and therefore dissipation.

As predicted by equation (3.11), the inclination angle also shows a strong z -dependence. Due to the finite size of the particles located near the centreplane of the Poiseuille flow, θ cannot be directly compared to that in a simple shear flow. Therefore, the inclination angles in the central region show strong deviations from the analytic solution.

Comparing the data for a single particle and the suspensions, we generally observe that collective effects lead to a decrease of the deformation parameter and an increase of the inclination angle, in particular for larger values of Re . This may have additional non-linear feedback effects on the lateral particle distributions.

4. Summary and conclusions

We have performed three-dimensional computer simulations of a particle suspension using a finite-element-immersed-boundary-lattice-Boltzmann method to investigate the interplay of fluid inertia and particle deformability in a planar Poiseuille flow. The channel Reynolds number Re and the particle capillary number Ca are used as free control parameters ($Re \in [3, 417]$, $Ca \in [0.003, 0.3]$) while the suspension volume fraction ϕ and channel confinement χ are kept fixed ($\phi = 0.1$, $\chi = 0.20$). Additionally we have performed reference simulations for a single particle ($\phi = 0.001$) under otherwise identical conditions.

We found that the Segré-Silberberg effect (Segré & Silberberg 1962*a,b*) is suppressed upon an increase of the particle deformability. While the concentration profile of the nearly rigid particles ($Ca = 0.003$) shows a central depletion region and a distinct peak in the vicinity of the walls for $Re \approx 30$ – 200 , the central depletion region for more deformable particles ($Ca > 0.03$) at fixed Re vanishes, and the lateral particle distribution becomes more narrow. We therefore conclude that the deformability-induced centrewards migration eventually exceeds the inertial lift force. This view is supported by the behaviour of a single particle; in particular, the particle for $Re = 6$ and $Ca = 0.3$ (*i.e.*, for minimum inertia and maximum deformability effect) assumes a lateral equilibrium position on the centreplane while all other particles end up at finite distances.

Another peculiar suspension behaviour has been found when both Re and Ca are large. For $Re > 200$ and $Ca > 0.03$, a particle focusing towards the centreplane takes place which is much stronger than the focusing caused by deformability alone (*i.e.* for large Ca and small Re). This effect is partly caused by the tendency of a single particle to move closer to the centreplane when Re becomes larger than about 45 as already observed by Shin & Sung (2011). But also the role of particle-particle interactions at finite volume fractions is important. We observe a reduction of the lateral particle velocity fluctuations, indicating a decrease of dispersion forces, when both Re and Ca are large. This is in line with results obtained by Doddi & Bagchi (2008*a*) who described a change of the nature of particle collisions and consequential reduction of dispersion in this parameter regime. However, to the best of our knowledge, the inertial focusing in a non-dilute deformable particle suspension in Poiseuille flow has not been described before.

We have also seen that the local suspension viscosity decreases with Ca but increases with Re . The former effect is well-known and caused by reduced flow resistance of soft particles while the latter finding can be explained by analysing the particle properties in the suspension. Both the particle deformation and inclination increase with Re , which is in agreement with results previously published by other groups (Doddi & Bagchi 2008*a*; Kim & Lai 2012; Laadhari *et al.* 2012). More strongly inclined particles lead to an

apparent growth of the volume fraction, which in turn increases the local dissipation. The inertia-augmented deformation may be one explanation for the strong inward migration of deformable particles at high Reynolds numbers.

Despite the growth of the local viscosity with Re , the inertial focusing of particles towards the centreplane leads to situations where the apparent viscosity of the overall suspension decreases. The decrease of the dissipation due to particles being shifted from the high-dissipation region near the wall to the low-stress region at the centreplane can overcompensate the local viscosity growth when Re is increased.

Generally, the interplay of velocity curvature (*i.e.* non-uniform stress), flow confinement, inertia-augmented particle deformation and inertia-dependent particle interactions leads to a complex suspension behaviour and non-homogeneous lateral particle distributions which in turn affects the rheology of the suspension. It is highly non-trivial to disentangle cause and effect of the observed phenomena in the present geometry. The large number of parameters forced us to reduce the dimensionality of the parameter space. Additional studies are required to investigate the relative contributions of the above-mentioned mechanisms and the effect of the confinement and volume fraction on the inertial focusing. We hope that this work will stimulate further experimental and theoretical investigations of deformability- and inertia-induced effects in suspension flows.

We thank Phillippe Peyla and Michael D. Graham for stimulating discussions, NWO/STW (VIDI grant 10787 of J. Harting) for financial support, and SARA Amsterdam for access to high performance computing resources (grant SH-235-13). We also thank the anonymous referees who provided constructive and valuable comments.

REFERENCES

- AIDUN, CYRUS K. & CLAUSEN, JONATHAN R. 2010 Lattice-boltzmann method for complex flows. *Annu. Rev. Fluid Mech.* **42**, 439–472.
- ASMOLOV, EVGENY S. 1999 The inertial lift on a spherical particle in a plane poiseuille flow at large channel reynolds number. *J. Fluid Mech.* **381**, 63–87.
- BAGCHI, PROSENJIT & KALLURI, R. MURTHY 2010 Rheology of a dilute suspension of liquid-filled elastic capsules. *Phys. Rev. E* **81** (5), 056320.
- BARTHÈS-BIESEL, D. 1980 Motion of a spherical microcapsule freely suspended in a linear shear flow. *J. Fluid Mech.* **100** (04), 831–853.
- BARTHÈS-BIESEL, D. & RALLISON, J. M. 1981 The time-dependent deformation of a capsule freely suspended in a linear shear flow. *J. Fluid Mech.* **113**, 251–267.
- CHARRIER, J. M., SHRIVASTAVA, S. & WU, R. 1989 Free and constrained inflation of elastic membranes in relation to thermoforming — non-axisymmetric problems. *J. Strain Anal. Eng.* **24** (2), 55–74.
- CHEN, YENG-LONG 2014 Inertia- and deformation-driven migration of a soft particle in confined shear and poiseuille flow. *RSC Advances* **4** (34), 17908–17916.
- CHUN, B. & LADD, A. J. C. 2006 Inertial migration of neutrally buoyant particles in a square duct: An investigation of multiple equilibrium positions. *Phys. Fluids* **18** (3), 031704–031704–4.
- COUPIER, GWENNOU, KAOUI, BADR, PODGORSKI, THOMAS & MISBAH, CHAOUQI 2008 Noninertial lateral migration of vesicles in bounded poiseuille flow. *Phys. Fluids* **20** (11), 111702–111702–4.
- DANKER, GERRIT, VLAHOVSKA, PETIA M. & MISBAH, CHAOUQI 2009 Vesicles in poiseuille flow. *Phys. Rev. Lett.* **102** (14), 148102.
- DI CARLO, DINO 2009 Inertial microfluidics. *Lab Chip* **9** (21), 3038–3046.
- DODDI, SAI K. & BAGCHI, PROSENJIT 2008a Effect of inertia on the hydrodynamic interaction between two liquid capsules in simple shear flow. *Int. J. Multiphas. Flow* **34** (4), 375–392.
- DODDI, SAI K. & BAGCHI, PROSENJIT 2008b Lateral migration of a capsule in a plane poiseuille flow in a channel. *Int. J. Multiphas. Flow* **34** (10), 966–986.

- ECKSTEIN, EUGENE C., BAILEY, DOUGLAS G. & SHAPIRO, ASCHER H. 1977 Self-diffusion of particles in shear flow of a suspension. *J. Fluid Mech.* **79** (01), 191–208.
- FAHRAEUS, R. & LINDQVIST, T. 1931 The viscosity of blood in narrow capillary tubes. *Am. J. Physiol.* **96**, 562–568.
- FARUTIN, ALEXANDER & MISBAH, CHAOUQI 2013 Analytical and numerical study of three main migration laws for vesicles under flow. *Phys. Rev. Lett.* **110** (10), 108104.
- GEISLINGER, T. M., EGGART, B., BRAUNMÜLLER, S., SCHMID, L. & FRANKE, T. 2012 Separation of blood cells using hydrodynamic lift. *Appl. Phys. Lett.* **100** (18), 183701–183701–4.
- HELFRICH, W. 1973 Elastic properties of lipid bilayers: theory and possible experiments. *Z. Naturforsch. C* **28** (11), 693–703.
- HUMPHRY, KATHERINE J., KULKARNI, PANDURANG M., WEITZ, DAVID A., MORRIS, JEFFREY F. & STONE, HOWARD A. 2010 Axial and lateral particle ordering in finite reynolds number channel flows. *Phys. Fluids* **22** (8), 081703–081703–4.
- HUR, SOOJUNG CLAIRE, HENDERSON-MACLENNAN, NICOLE K., MCCABE, EDWARD R. B. & CARLO, DINO DI 2011 Deformability-based cell classification and enrichment using inertial microfluidics. *Lab Chip* **11** (5), 912–920.
- HUR, SOOJUNG CLAIRE, TSE, HENRY TAT KWONG & CARLO, DINO DI 2010 Sheathless inertial cell ordering for extreme throughput flow cytometry. *Lab Chip* **10** (3), 274–280.
- KAOU, BADR, COUPIER, GWENNOU, MISBAH, CHAOUQI & PODGORSKI, THOMAS 2009 Lateral migration of vesicles in microchannels: effects of walls and shear gradient. *La Houille Blanche* (5), 112–119.
- KAOU, B., RISTOW, G. H., CANTAT, I., MISBAH, C. & ZIMMERMANN, W. 2008 Lateral migration of a two-dimensional vesicle in unbounded poiseuille flow. *Phys. Rev. E* **77** (2), 021903.
- KILIMNIK, ALEX, MAO, WENBIN & ALEXEEV, ALEXANDER 2011 Inertial migration of deformable capsules in channel flow. *Phys. Fluids* **23** (12), 123302–6.
- KIM, YONGSAM & LAI, MING-CHIH 2012 Numerical study of viscosity and inertial effects on tank-treading and tumbling motions of vesicles under shear flow. *Phys. Rev. E* **86** (6), 066321.
- KRÜGER, T., FRIJTERS, S., GÜNTHER, F., KAOU, B. & HARTING, J. 2013 Numerical simulations of complex fluid-fluid interface dynamics. *The European Physical Journal Special Topics* **222** (1), 177–198.
- KRÜGER, T., VARNIK, F. & RAABE, D. 2011 Efficient and accurate simulations of deformable particles immersed in a fluid using a combined immersed boundary lattice boltzmann finite element method. *Comput. Method. Appl.* **61** (12), 3485–3505.
- LAADHARI, AYMEN, SARAMITO, PIERRE & MISBAH, CHAOUQI 2012 Vesicle tumbling inhibited by inertia. *Phys. Fluids* **24** (3), 031901–031901–7.
- LADD, ANTHONY J. C. 1994 Numerical simulations of particulate suspensions via a discretized boltzmann equation. part 1. theoretical foundation. *J. Fluid Mech.* **271**, 285–309.
- LEAL, L. G. 1980 Particle motions in a viscous fluid. *Annu. Rev. Fluid Mech.* **12**, 435–476.
- LI, XIAOFAN & POZRIKIDIS, C. 2000 Wall-bounded shear flow and channel flow of suspensions of liquid drops. *Int. J. Multiphas. Flow* **26** (8), 1247–1279.
- LUO, ZHENG YUAN, WANG, SHU QI, HE, LONG, XU, FENG & BAI, BO FENG 2013 Inertia-dependent dynamics of three-dimensional vesicles and red blood cells in shear flow. *Soft Matter* .
- MARTEL, JOSEPH M & TONER, MEHMET 2012 Inertial focusing dynamics in spiral microchannels. *Phys. Fluids* **24** (3), 32001.
- MATAS, JEAN-PHILIPPE, MORRIS, JEFFREY F. & GUZZELLI, ÉLISABETH 2004 Inertial migration of rigid spherical particles in poiseuille flow. *J. Fluid Mech.* **515**, 171–195.
- MUNN, LANCE L. & DUPIN, MICHAEL M. 2008 Blood cell interactions and segregation in flow. *Ann. Biomed. Eng.* **36** (4), 534–544.
- NOURBAKHS, AMIREH, MORTAZAVI, SAEED & AFSHAR, YASER 2011 Three-dimensional numerical simulation of drops suspended in poiseuille flow at non-zero reynolds numbers. *Phys. Fluids* **23** (12), 123303–11.
- PESKIN, CHARLES S. 2002 The immersed boundary method. *Acta Numerica* **11**, 479–517.
- PRANAY, PRATIK, HENRÍQUEZ-RIVERA, RAFAEL G. & GRAHAM, MICHAEL D. 2012 Depletion

- layer formation in suspensions of elastic capsules in newtonian and viscoelastic fluids. *Phys. Fluids* **24** (6), 061902–061902–30.
- SALAC, DAVID & MIKSI, MICHAEL J. 2012 Reynolds number effects on lipid vesicles. *Journal of Fluid Mechanics* **711**, 122–146.
- SCHONBERG, JEFFREY A. & HINCH, E. J. 1989 Inertial migration of a sphere in poiseuille flow. *J. Fluid Mech.* **203**, 517–524.
- SEGRÉ, G. & SILBERBERG, A. 1962*a* Behaviour of macroscopic rigid spheres in poiseuille flow part 1. determination of local concentration by statistical analysis of particle passages through crossed light beams. *J. Fluid Mech.* **14** (01), 115–135.
- SEGRÉ, G. & SILBERBERG, A. 1962*b* Behaviour of macroscopic rigid spheres in poiseuille flow. part 2. experimental results and interpretation. *J. Fluid Mech.* **14**, 136–157.
- SHAN, XIAOWEN & DOOLEN, GARY 1995 Multicomponent lattice-boltzmann model with inter-particle interaction. *J. Stat. Phys.* **81** (1), 379–393.
- SHI, LINGLING, PAN, TSORNG-WHAY & GLOWINSKI, ROLAND 2012 Lateral migration and equilibrium shape and position of a single red blood cell in bounded poiseuille flows. *Phys. Rev. E* **86** (5), 056308.
- SHIN, SOO JAI & SUNG, HYUNG JIN 2011 Inertial migration of an elastic capsule in a poiseuille flow. *Phys. Rev. E* **83** (4), 046321.
- SHIN, SOO JAI & SUNG, HYUNG JIN 2012 Dynamics of an elastic capsule in moderate reynolds number poiseuille flow. *Int. J. Heat Fluid Fl.* **36** (0), 167–177.
- SKALAK, R., TOZEREN, A., ZARDA, R.P. & CHIEN, S. 1973 Strain energy function of red blood cell membranes. *Biophys. J.* **13** (3), 245–264.
- SUCCI, SAURO 2001 *The Lattice Boltzmann Equation for Fluid Dynamics and Beyond*. Oxford University Press.
- TANAKA, TATSUYA, ISHIKAWA, TAKUJI, NUMAYAMA-TSURUTA, KEIKO, IMAI, YOHISUKE, UENO, HIRONORI, MATSUKI, NORIYAKI & YAMAGUCHI, TAKAMI 2012 Separation of cancer cells from a red blood cell suspension using inertial force. *Lab Chip* **12** (21), 4336–4343.
- YAZDANI, ALIREZA Z. K., KALLURI, R. MURTHY & BAGCHI, PROSENJIT 2011 Tank-treading and tumbling frequencies of capsules and red blood cells. *Phys. Rev. E* **83** (4), 046305.
- ZURITA-GOTOR, M., BŁAWZDZIEWICZ, J. & WAJNRYB, E. 2012 Layering instability in a confined suspension flow. *Phys. Rev. Lett.* **108** (6), 068301.